




Article

Refined Coseismic Slip Model and Surface Deformation of the 2021 Maduo Earthquake: Implications for Sensitivity of Rupture Behaviors to Geometric Complexity

Xiaoli Liu ¹, Debeier Deng ¹, Zhige Jia ¹, Jing Liu-Zeng ^{2,*} , Xinyu Mo ¹, Yu Huang ¹, Qiaozhe Ruan ¹ and Juntao Liu ¹

¹ Institute of Seismology, China Earthquake Administration, Wuhan 430071, China; liuxl.j@163.com (X.L.); 2017301610203@whu.edu.cn (D.D.); jia.zg@126.com (Z.J.); 2018302140014@whu.edu.cn (X.M.); m18848272822@163.com (Y.H.); ruanqiaozhe23@mails.ucas.ac.cn (Q.R.); liu127186@163.com (J.L.)

² School of Earth System Science, Tianjin University, Tianjin 300072, China

* Correspondence: liu_zeng@tju.edu.cn

Abstract: Geometric complexities of a fault system have a significant impact on the rupture behavior of the fault. The 2021 Mw7.4 Maduo earthquake occurred on a multi-segmented complex sinistral fault in the interior of the Bayan-Har block in the northern Tibetan Plateau. Here, we integrate centimeter-resolution surface rupture zones and Sentinel-2 optical displacement fields to accurately determine the geometric parameters of the causative fault in detail. An adaptive quadtree down-sampling method for interferograms was employed to enhance the reliability of the coseismic slip model inversion for interferograms. The optimal coseismic slip model indicated a complex non-planar structure with varying strike and dip angles. The largest slip of ~6 m, at a depth of ~7 km, occurred near a 6 km-wide stepover (a geometric complexity area) to the east of the epicenter, which occurred at the transition zone from sub-shear to super-shear rupture suggested by seismological studies. Optical and SAR displacement fields consistently indicated the local minimization of effective normal stress on releasing stepovers, which facilitated rupture through them. Moreover, connecting intermediate structures contributes to maintaining the rupture propagation through wide stepovers and may even facilitate the transition from subshear to supershear. Our study provides more evidence of the reactivation of a branched fault at the western end during the mainshock, which was previously under-appreciated. Furthermore, we found that a strong asymmetry in slip depth, stress drop, and rupture velocity east and west of the epicenter was coupled with variations in geometric and structural characteristics of fault segments along the strike. Our findings highlight the sensitivity of rupture behaviors to small-scale details of fault geometry.

Keywords: 2021 Maduo earthquake; coseismic slip model; optical surface deformation; phase gradient; stepover; bifurcation; rupture behavior



Citation: Liu, X.; Deng, D.; Jia, Z.; Liu-Zeng, J.; Mo, X.; Huang, Y.; Ruan, Q.; Liu, J. Refined Coseismic Slip Model and Surface Deformation of the 2021 Maduo Earthquake: Implications for Sensitivity of Rupture Behaviors to Geometric Complexity. *Remote Sens.* **2024**, *16*, 713. <https://doi.org/10.3390/rs16040713>

Academic Editor: Alessandro Bonforte

Received: 20 November 2023

Revised: 2 February 2024

Accepted: 7 February 2024

Published: 18 February 2024



Copyright: © 2024 by the authors. Licensee MDPI, Basel, Switzerland. This article is an open access article distributed under the terms and conditions of the Creative Commons Attribution (CC BY) license (<https://creativecommons.org/licenses/by/4.0/>).

1. Introduction

The Bayan-Har Block is the most seismically active region, experiencing all earthquakes above M 7.0 that have occurred in recent years in the Tibetan Plateau and even in China. Since the 1976 Tangshan earthquake, all major earthquakes in mainland China have occurred in or around this region (see Figure 1), including the 2001 Mw 7.8 Kokoxili earthquakes, the 2008 Mw 7.2 Yutian earthquake, the 2008 Mw 7.9 Wenchuan earthquake, the 2010 Mw 6.9 Yushu earthquake, the 2013 M 7.0 Lushan earthquake, and the 2014 Mw 6.9 Yutian earthquake. These temporally clustered earthquakes occurred along the boundary fault zones with high slip rates, indicating synchronized activity of their seismogenic faults. However, the most recent Mw7.4 Maduo earthquake on 21 May 2021 occurred on an unknown secondary fault within the block, which was named the Jianguo fault after the earthquake. It is an immature fault with low seismicity rates [1], a slow slip rate [2],

and a long seismic recurrence interval [3]. The Maduo earthquake caused a 158-km-long surface rupture [3–6], which was larger than that estimated by the empirical relationship of moment magnitude versus surface rupture length proposed by Well et al. [7].

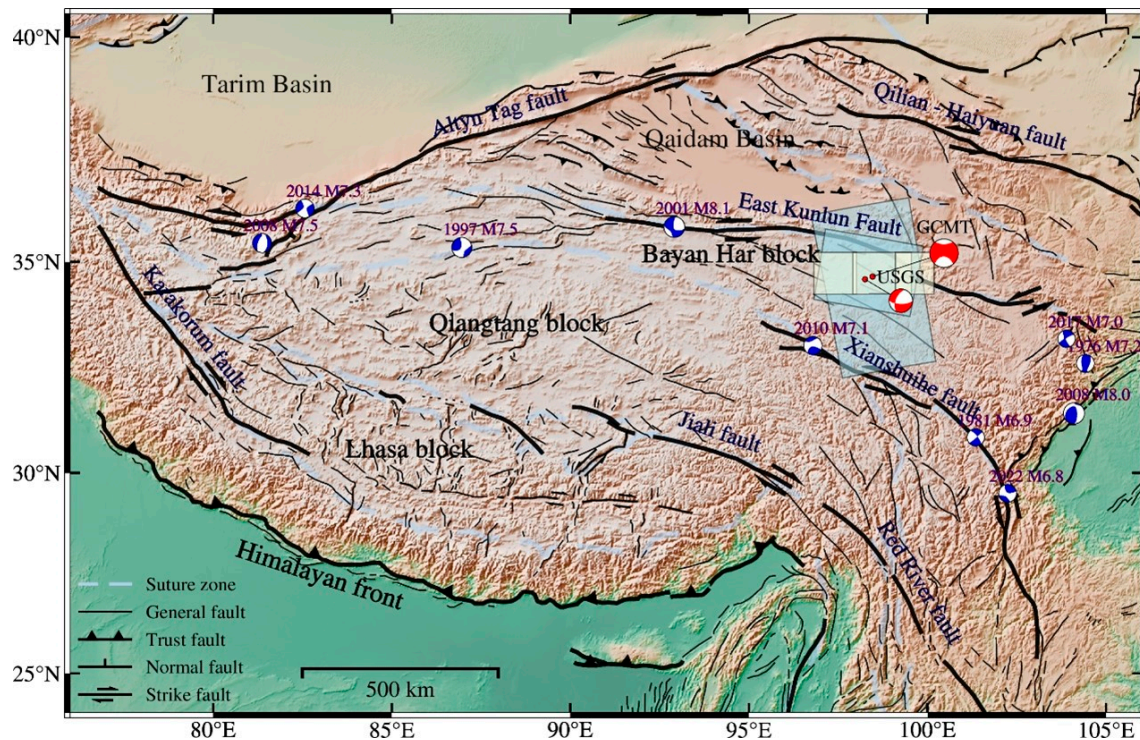


Figure 1. Topographic and tectonic setting map of the Tibetan plateau. Gray dashed lines and thick black and thin lines indicate block suture zones and main and secondary active faults, respectively [8]. Blue/white and red/white beach balls denote focal mechanisms of historical and Maduo earthquakes ($M \geq 7$) in the Bayan-Har block reported in the Global CMT (GCMT) and USGS catalog from 1 January 1966 to 1 June 2021, respectively. The light blue and yellow boxes depict footprints of SAR and optical images used in this study, respectively.

The Maduo earthquake involved a bilateral rupture with varying rupture speeds on either side of the epicenter. This has been confirmed by various seismic and geodetic inversions as well as the aftershock sequence [9–14]. However, there are still many aspects that require further understanding. For instance, two entirely contradictory conclusions on fault maturity from different datasets [15,16]. So far, four representative coseismic slip models have emerged from published research with seismological, geodetic, or jointed inversions [10,13,14,17–19]. These models differ in fault geometry and slip distribution [9,18]. For example, the GNSS coseismic slip model assumes a homogeneous elastic half-space with a dip toward the north and reveals two asperities on either side of the epicenter [19]. Wei et al. collectively utilized geodetic data, nearby high-rate GPS waveforms, regional broadband waveforms, and teleseismic body waves to perform joint inversion, employing an eight-segment fault model. The result revealed a tail-end bifurcation at the eastern end [9]. Guo et al. suggest that a northwest-trending tail-end bifurcation at the western end contributes to coseismic deformation [17]. Different results on the distribution of coseismic slip [13,16,18,20] may further hamper our understanding of fault properties, rupture dynamics, and mechanisms.

Accurately characterizing details of near-fault surface deformation is essential for reliable coseismic slip inversions to constrain spatial patterns of coseismic slip. However, the radar phase is often decorrelated in the vicinity of the rupture trace for large earthquakes [21]. For this reason, incorporating additional near-field observations and more detailed fault geometries is considered to improve the issue [22]. For example, Xu et al. [21]

enhanced the static coseismic slip inversion for three $M_w > 7$ strike-slip earthquakes by integrating global positioning system, radar, and optical satellite observations. They refined the radar data processing and utilized more detailed, geologically constrained fault geometries. For the Maduo earthquake, He et al. [18] utilized optical deformation derived from Sentinel-2 images to identify the surface trace of the seismogenic fault. This approach effectively minimized the uncertainty of the slip model and suggested that a blind fault may have ruptured seismically near Eling Lake. This has yet to be confirmed because it was not present in other models [13,16,23].

To gain a deeper understanding of the complexity of the seismogenic fault associated with the 2021 Maduo earthquake, we improved the surface mapping trace of the seismogenic fault using the detailed surface rupture data interpreted based on centimeter-resolution aerial images and employed a more sophisticated InSAR data processing with an adaptive quadtree down-sampling and an on-fault correlation mask. We provide more details of the fault geometry and coseismic slip distribution and incorporate additional near-fault deformation data obtained from optical deformation fields and full-resolution phase gradient fields, allowing for a discussion of new findings on fault properties and earthquake physics.

2. Data Preparation

In this study, we utilized three types of datasets (Table S1 in Supporting Information), comprising Sentinel-1 C-band SAR data and Sentinel-2 optical satellite images provided by the European Space Agency (ESA), Paris, France and centimeter-resolution Unmanned Aerial Vehicle (UAV) aerial images collected during the first two weeks after the Maduo mainshock [4,6]. The spatial coverage of these images is depicted in Figure 1. The post-earthquake SAR images were captured as early as the fourth day following the mainshock, during which there were no significant aftershocks ($M > 5$), then the postseismic deformation was negligible in comparison to the coseismic deformation [18].

2.1. Optical Deformation Processing

Coseismic surface rupture zones are the most direct evidence of fault rupture exposure at the surface. They provide important, albeit incomplete, information about the fault systems that produce large earthquakes and help to constrain the seismic source parameters [24]. To map the surface ruptures of the 2021 Maduo earthquake in detail, beyond two field investigations, we conducted UAV (Unmanned Aerial Vehicle) aerial photogrammetry to obtain centimeter-resolution images (with a pixel size of 3–6 cm along the strike and 10 cm across the fault, respectively) in the earthquake emergency period and the second year after the earthquake, respectively. These data almost cover the entire rupture zone, which has a width of 1.2–1.5 km along the strike and 10 km across the fault. Using ArcGIS 10.1 and Agisoft Metashape Pro v2.0, we conducted additional orthorectification, image filtering, and cloud masking and reprojected the data into the Universal Transverse Mercator (UTM) to create georeferenced Digital Orthorectified Maps (DOMs) and the corresponding Digital Elevation Model (DEM) with a resolution of 3–5 cm. Using the UAV-derived DOMs and DEMs; we obtained a detailed surface rupture structure spanning 158 km length, which exhibits a clear en echelon rupture pattern [4] (see Figure 2).

In addition, to examine the spatial distribution of the coseismic displacements on a large scale, we conducted the Sub-Pixel Correlation process on band 8 of Sentinel-2 images (refer to Table S1 in the Supporting Information) before and after the mainshock using the COSI-Corr 2014 [25]. The COSI-Corr 2014 enables the precise orthorectification of images by applying topographic correction using a high-resolution digital elevation model and ground control points. Considering that the resolution of Sentinel-2 images is 10 m, we selected DEM data with a resolution of 12.5 m. After applying masking and smoothing filters, the signal-to-noise ratio was improved (see Figure S1 in the Supporting Information). Additionally, a first-order polynomial surface fitting model was utilized to eliminate orbit errors and band errors. The sliding window size was set at 32×32 pixels, with a step size

of 10 pixels (approximately 30 m resolution), and the robustness iteration was set at 4 times. Finally, the displacement maps in the EW and NS directions (Figure 3a,b) were generated with an accuracy of 1/10 of the pixel size of the input image [26].

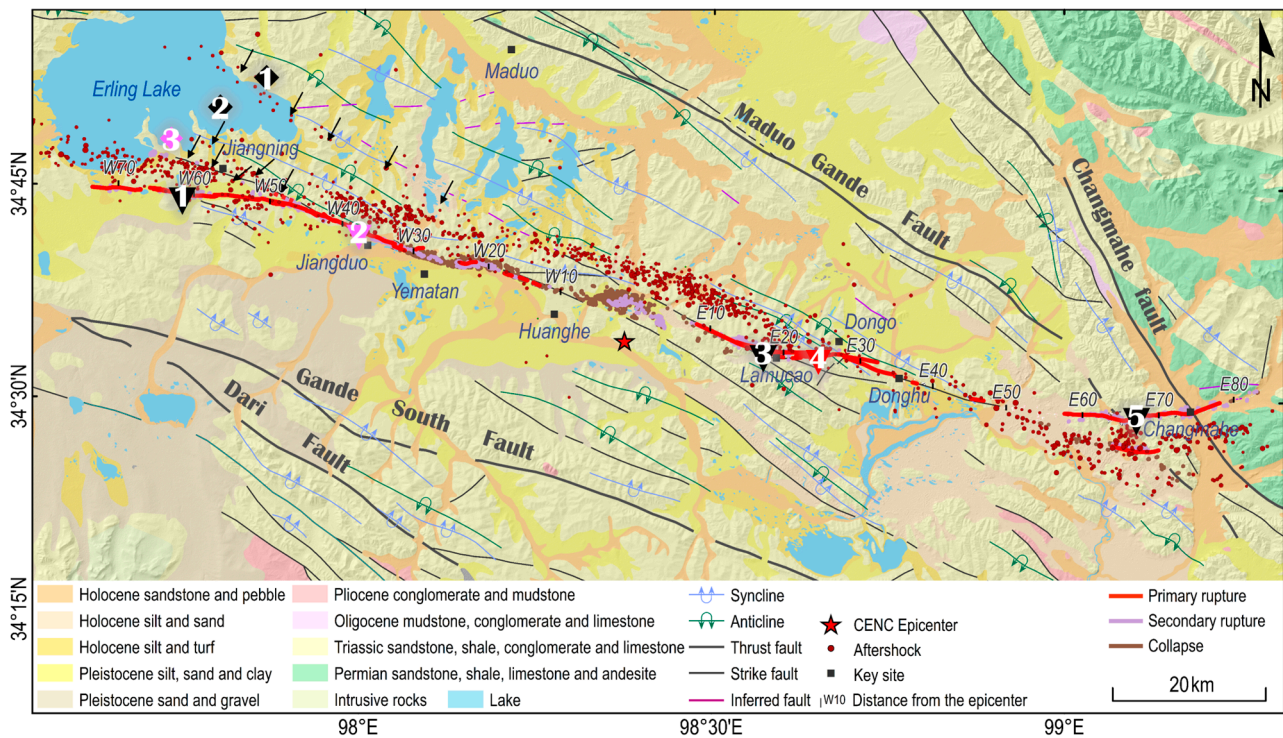


Figure 2. Surface rupture map of the 2020 Madoi earthquake, with relocated aftershocks 8 days after the main earthquake [14]. Inverted triangles with numbers indicate the projected position of the maximum slip of every asperity on the surface. Diamonds with numbers indicate possible projected positions of the west branch on the surface.

2.2. Phase Gradient Processing

Compared with the same resolution phase gradient field, the deformation field extracted from Sentinel-1 A/B images was too smooth, which was insufficient for outlining more detailed, geologically constrained fault geometries. For more detailed information on smaller-scale features, Xu et al. directly derived the phase gradient of the Ridgecrest earthquake directly from the real ($R(x)$) and imaginary ($I(x)$) of the full-resolution interferograms based on the multi-track Sentinel-1 images [27]. In this study, the position vector x comprises the range and azimuth coordinates of the interferogram. The authors mapped the main rupture zone and hundreds of small fractures surrounding the earthquake [28].

We obtained the full-resolution phase gradient maps using the method proposed by [29]. Since a single ascending Sentinel-1 image cannot cover the entire study area, we compiled three sets of Sentinel-1 descending images taken before and within one month after the earthquake. Using the GMTSAR 6.1 [29], the specific data processing process includes the following steps: (1) registering and resampling the SLC image and removing the orbit error and flat-earth effect based on the precision orbit and a 30 m resolution DEM; (2) applying Goldstein phase filtering and multi-looking processing to generate complex phase interferograms with a high SNR for each group; (3) extracting the azimuth and range phase gradients from the full-resolution complex phase interferograms; (4) stacking azimuth and range phase gradients, respectively, to produce final azimuth and range phase gradient maps through averaging; and (5) filtering with a 41×41 Gaussian filter and geocoding the result to the geographic WGS-84 coordinate system (approximately 20 m) (Figure 3c,d).

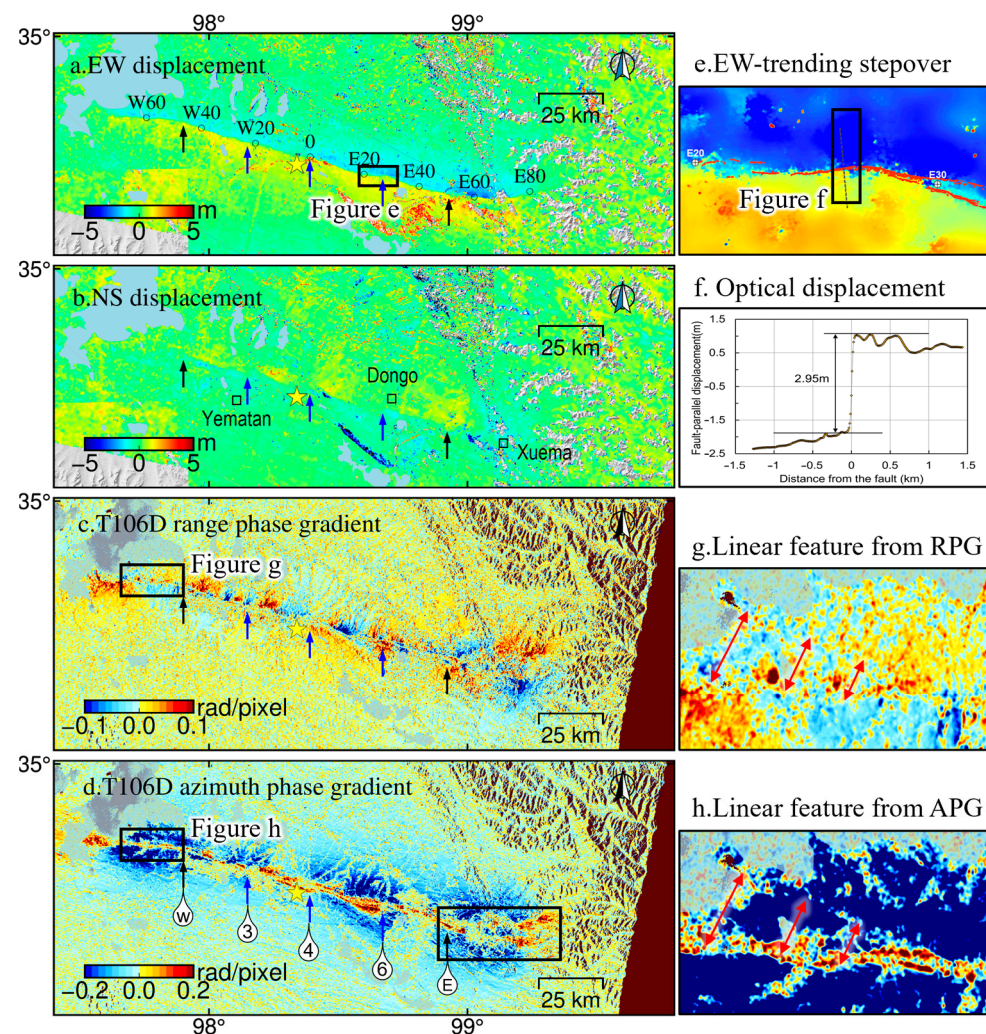


Figure 3. Full-resolution phase gradient and optical deformation fields. (a) EW- and (b) NS-deformation maps, (c) descending range and (d) azimuth phase gradient maps, (e) EW-trending stepover, (f) Optical displacement, and (g,h) linear features from the range and azimuth phase gradients. The yellow star indicates the CENC epicenter. W20 in Panel (a) indicates 20 km west of the CENC epicenter. Black hollow squares and rectangles mark sites and tail bifurcations, respectively. Black and blue arrows mark the locations of bends and stepovers along the main fault, respectively. Numbers in drop-shaped signs show stepover width.

2.3. Three-Dimensional (3D) Displacement Processing

Here, we employed the traditional two-pass Differential Interferometric Synthetic Aperture Radar (D-InSAR) method and GMTSAR 6.1 [29] software to process two sets of ascending and one set of descending images. We registered and resampled the SLC images in Table S1 and then corrected for the orbit errors and the flat-earth effect using precision orbit and SRTM3 DEM data with a resolution of 30 m. We performed the multi-looking operations and Goldstein phase filtering. Finally, we used the SNAPU method to unwrap the interferogram of the ascending and descending tracks, respectively (see Figures S2 and S3 in the Supporting Information). We utilized the Generic Atmospheric Correction Online Service for InSAR (GACOS) atmospheric correction data [30,31] to eliminate the atmospheric delay error from geocoded interferograms.

D-InSAR can only capture the projection of actual surface deformation in the one-dimensional Line of Sight (LoS) direction [32], which can result in the underestimation and misinterpretation of surface deformation [33]. The open-source GMTSAR software [29] offers a sophisticated offset-tracking script for generating more detailed azimuth displace-

ment. To achieve this, we utilized the Weighted Least Squares (WLS) method [34] to establish the projection relationship (Equation (1)) between the one-dimensional LoS deformation and the three-dimensional surface deformation vector [35]. Based on the LoS and azimuth displacement data from the ascending and descending tracks, we obtained the three-dimensional co-seismic deformation for this earthquake.

$$\begin{aligned} u_{LOS} &= u_n \cdot s_n + u_e \cdot s_e + u_v \cdot s_v = u_n \cdot \sin\varphi \sin\theta - u_e \cdot \cos\varphi \sin\theta + u_v \cdot \cos\theta + \delta_{u_{LOS}} \\ u_{AZO} &= u_n \cdot s_n + u_e \cdot s_e = u_n \cos\varphi + u_e \sin\varphi + \delta_{u_{AZO}} \end{aligned} \quad (1)$$

Here, u_n , u_e , and u_v are the north-south, east-west, and vertical surface deformation components, respectively. φ is the azimuth of the satellite orbit; θ is the incidence angle of the satellite orbit; $\delta_{u_{LOS}}$ is the error of the observation in the LoS direction; and $\delta_{u_{AZO}}$ is the error of the azimuth observation.

The retrieval of deformation information from the surface rupture zone near the fault is beneficial for analyzing the mechanism of seismogenic faults and explaining the characteristics of earthquake deformation. Beyond the decoherent region, the deformations in other regions are approximately consistent.

In Figure 4a,b, the unwrapped coseismic deformation fields of ascending and descending tracks exhibit a clear antisymmetric pattern in the LoS direction with similar amplitudes of 85 cm and 76 cm, respectively. It indicates a significant left-lateral strike-slip motion along the seismogenic fault. Similar to the optical and phase gradient results, we observed variations in the rupture strike, particularly at the western and eastern tails. It shows the complexity of fault geometry.

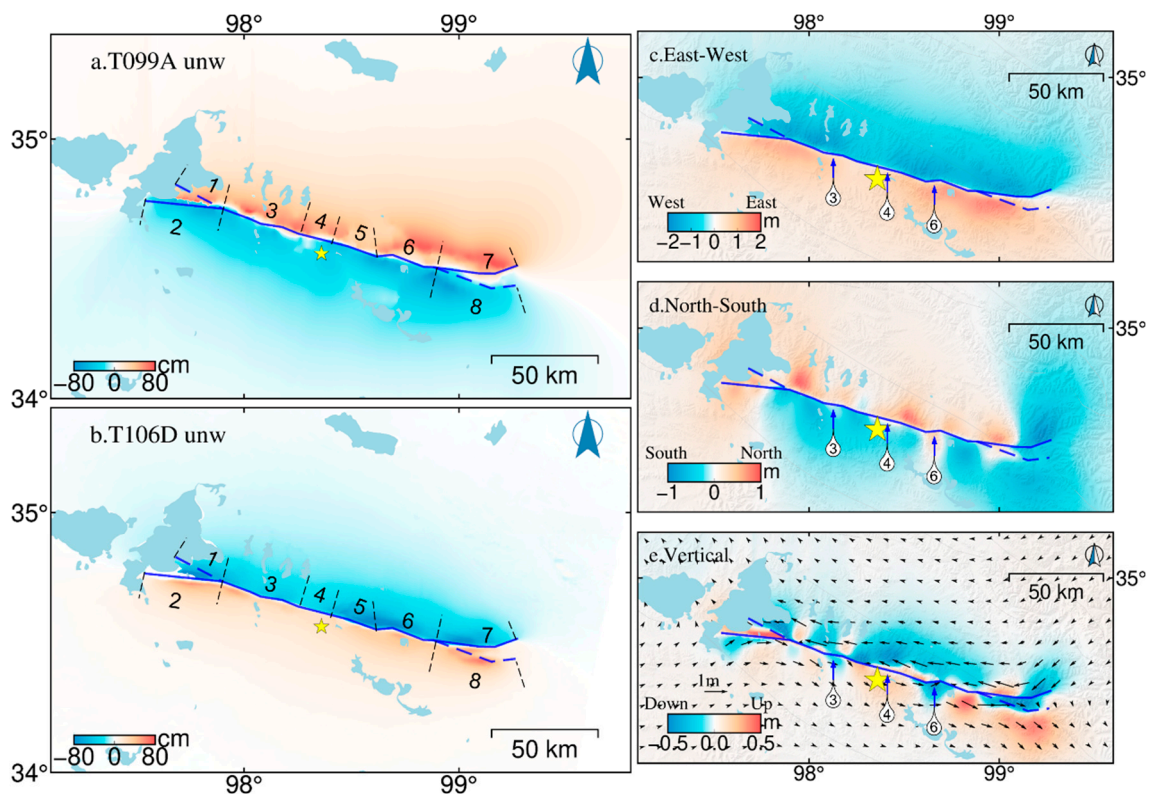


Figure 4. Coseismic LoS direction deformation and three-dimensional displacement fields for the 2021 Maduo earthquake. (a) Ascending, (b) Descending, (c) EW-, (d) NS-, and (e) Vertical-component displacement fields. The yellow star indicates the epicenter. Blue solid and dashed lines represent the main and branch faults, respectively, divided into 8 segments. The caption is as for Figure 3.

In Figure 4c–e, the 3D displacement fields clearly show that the magnitude of the EW displacements is far greater than those in the NS and vertical directions. The long-

wavelength EW deformation is significant, reaching up to 4 m. The amplitude of the deformation in the western and eastern parts is larger than in the epicenter region (see Figure 4c). This difference may arise from the slow rupture speed in the beginning stage [12]. The middle-wavelength NS deformation mainly occurred in near-fault zones, with the amplitude varying along the strike, reaching a maximum of 2 m (see Figure 4d). Vertical deformation was only observed in the near-fault zones, with smaller amplitudes and an alternating sign along the strike (see Figure 4e).

2.4. Interferogram Down-Sampling

Due to near-field decoherence and misfit displacements affected by the local complexity of fault geometry, the traditional quadtree down-sampling algorithm based on a single variance threshold makes it difficult to balance the efficiency and accuracy of sampling, especially for regions with small deformation gradients or large background noise. For this reason, the InSAR interferograms were subsampled using the adaptive quadtree down-sampling method [36]. If both the deformation variance and gradient of the current window were less than the threshold, the window should no longer be subdivided; otherwise, the Sigmoid activation function (Equation (2)) of deformation variance, gradient, and coherence was used as the threshold for window partition. The final down-sampling result preserves significant displacement near faults as well as local and weak deformation features (Figure 5).

$$P = \frac{1}{1 - e^{\tau - 2 \cdot \tau \cdot \frac{(\alpha \cdot v + \beta \cdot g + \theta \cdot \gamma_k) - (\alpha \cdot T_v + \beta \cdot T_g + \theta \cdot T_\gamma)}{(1-\alpha) \cdot T_v + (1-\beta) \cdot T_g + (1-\theta) \cdot T_\gamma}}} \quad (2)$$

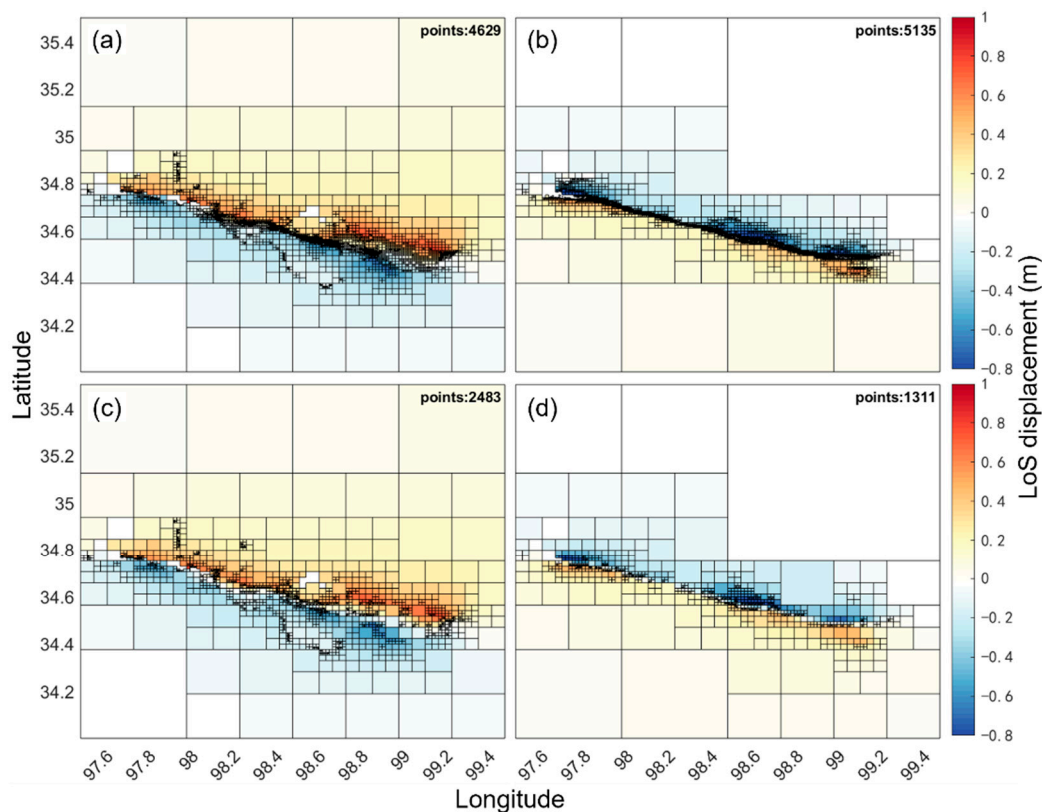


Figure 5. The downsampled results used the traditional variance method (a,b) and the adaptive threshold methods (c,d), respectively, for the ascending and descending interferograms.

Here, α , β , and θ are the weights of deformation variance, gradient, and coherence, respectively. T_v , T_g , and T_γ are the threshold for the three parameters α , β , and θ , respectively.

3. Result

3.1. Refined Fault Geometry

We observed significant differences in the surface traces of the seismogenic fault used in published finite-fault solutions, particularly in fault strikes, dips, and segments (see Figure 4) [9,10,12,13,23,37]. Some of these representations were overly simplified to misalign with the detailed surface rupture zone mapping based on UAV images [6]. To gain a better understanding of the impact of dip, strike, and tail bifurcation on inversion results, we assembled centimeter-resolution surface rupture zone mapping [6], optical EW and NS direction displacement (Figure 3a,b), azimuth and range phase gradient fields (Figure 3c,d), 3D displacement fields (Figure 4c–e), and 1:250,000 regional geological maps. This allowed us to cross-examine and better constrain the geometry parameters of the seismogenic fault. In Figures 3a and 4c, a notable linear trend is evident. A 110°-trending discontinuity separated the deformation field into two parts, clearly defining the projection of the main fault onto the surface. A similar pattern was observed in Figures 3b and 4d, but the signal amplitude was weak. The optical deformation indicates a significant left-lateral strike-slip motion linked to the Maduo event. Furthermore, the horizontal slip direction on the northern and southern walls of the fault was nearly parallel to the fault strike in a counterclockwise pattern (see Figure 4e). The closer to the fault, the larger the amplitude.

The representation of fault geometry discontinuities, such as fault stepovers, bends, and branches, was also well depicted, primarily through variations in the direction of the deformation gradient [28,38]. First, in Figure 3c, we observed that regions with alternating deformation signs always corresponded to the position of stepovers, bends, or triple junctions on the azimuth and phase gradient maps (near circles in Figure 3c). A similar pattern was observed in Figure 4e, with an alternating sign along the strike, indicating slight uplift or subsidence alternately occurring near the tails of the fault. This implies that faults can affect the vertical motion around bends [39]. Second, in comparison to the main fault strands, the NS components of stepovers with an EW-trending were consistently locally minimized (see Figures 3b and 4d). Considering the fault strike, this suggests that the effective normal stress decreased as the rupture passed through them, potentially enhancing the rupture's ability to jump [40]. Third, at the eastern and western ends of the seismogenic fault, we observed two linear features bending toward the northwest and southeast, respectively (highlighted as rectangular regions in Figures 3d and 4e), strongly suggesting triggering activity associated with fault branches [28]. By contrast, the linear feature on the eastern tail was more distinct than that on the western tail, which may indicate that the slip amplitude on the eastern branch was stronger than on the western branch, consistent with our field investigation [4,6]. Overall, the intricate pattern of the displacement fields derived from optical and radar datasets jointly indicates the geometric complexity of the seismogenic fault. It may be a complex non-planar structure with varying strikes and dips along its length, which is also advocated in recent studies using high-resolution fault trace and aftershock data [9,18,41].

Based on the surface rupture zone (see Figure 2) and optical deformation fields (see Figure 3), we divided the ruptured fault into eight segments with varying strike angles (mainly determined by the surface rupture zone mapping) and dip angles (using the parameters initially published by Wei et al. [9] as the basis for our static coseismic slip model (Table 1) (Figure 4).

Table 1. Geometric parameters of the eight-segment fault model used in the inversion.

Segment	1	2	3	4	5	6	7	8
Strike (°)	315	275	288	284	293	285	88	115
Dip (°)	73–78	73–78	75–85	75	75	80–90	78–83	78–83
Direction of dip			North			Vertical		South

3.2. Refined Coseismic Slip Distribution

We used the Steepest Descent Method (SDM) [42] to calculate the coseismic slip distribution. We constructed a layered Earth model [43] for the study area (Table S4) and calculated Green's functions. We discretized the fault plane into a series of $1.5 \text{ km} \times 1.5 \text{ km}$ rectangular subpatches with fixed fault depths of 0 km and 25 km at the top and bottom. According to the refined surface projection of the seismogenic fault, we synthesized the findings of previous studies [9], established initial fault parameters, and employed variable dips and strikes to search. This involved allowing the dip angle of the south dip and north dip fault segments to vary between 60° and 90° .

Due to the systematic errors in extracting the deformation from ascending and descending datasets, the weight for each dataset should be taken into consideration in the joint inversion process of the slip distribution model. A single ascending or descending dataset cannot fully cover the earthquake area, so it is necessary to splice images to create a complete deformation field. The splice lines of two overlapping images nearly align with the fault trace lines, dividing the north and south walls. The ascending dataset only covers the southeast corner of the deformation area. When using the same splicing method, the ascending dataset performed better than the descending dataset. However, the descending dataset completely covered the study area, while the ascending dataset did not. After careful consideration, we finally determined that the weight of the ascending/descending datasets = 1:1.

In contrast, the fitting degree of the best-fit model derived using the adaptive quadtree down-sampling method raised from 86~88% to 93%, and the model misfit decreased from 0.45 to 0.36 for the ascending and descending datasets, respectively, compared to the traditional method, while using fewer sampling data. After several iterations, we screened the model with the best fit and identified the optimal fault parameter settings (Table 2).

Table 2. Focal mechanism parameters of the 2021 Maduo earthquake.

Asperity	This Study								Wei et al. 2022 [9]	Zhao et al. 2021 [1]	He et al. 2021 [18]
	lon./°	lat./°	depth/km	Strike/°	Dip/°	Rake/°	Max_slip/m	Mw	Dip	Dip	Dip
M7	97.83	34.78	5.2	315	77N	34	1.6	6.52			83°S
M1	97.71	34.76	5.2	95	75N	−6	3.4	6.69	56°N	85°S	77°N
M2	98.00	34.71	5.2	108	81N	10	5.3	6.95	67°N	85°N	72°N
M3	98.57	34.57	3.7	110	85N	10	3.9	6.49	88°N		82°N
M4	98.66	34.55	6.9	105	90	7	6.0	6.87	81°N	85°N	
M5	99.11	34.47	6.8	88	81S	−7	4.3	6.85	89°S	80°N	90°
M6	99.98	34.47	5.3	115	82S	27	2.9	6.84	89°N	85°N	90°
Mw								7.35	FFM:7.44 MPS:7.42	7.38	7.43

To illustrate the extent to which the SAR images can constrain the resolution of the slip model and show uncertainties of the slip and trade-offs of slips between different patches, we conducted a checkerboard test [44] (Figure S6). Our resolution test thus demonstrated a reasonable resolution to retrieve the shallow, strike trend smooth asperities from low-slip zones, implying that the pattern of slip could be resolved under these conditions.

Parameterization of fault geometry affects the inferred slip distribution [9,18]. The dip direction of the seismogenic fault significantly affects the slip distribution of the model. A constant dip direction is more likely to result in larger seismic moments [45], especially when the dip direction of the tail bifurcations is the same as that of the main fault. For this reason, we varied the dip of each segment by $\pm 20^\circ$ from the vertical in 5° increments (refer to Table S2 in the Supporting Information). The best-fit model indicated that the coseismic rupture plane was a complex, high-dip, nonplane structure (see Figures 6 and 7). The fault plane of the west and east sides of the M4 dipped towards the north and south, respectively.

The dip angle of the east side was about 80–85°, which was steeper than the west side. The M4 was almost vertical. This may explain the differences between the different models (see Figure S5 and Table S3 in Supporting Information). A change in the dip direction of the fault (even with the same dip angle) may lead to significant limitations on rupture, especially in the transition zone of the dip direction, resulting in distinct slip distributions.

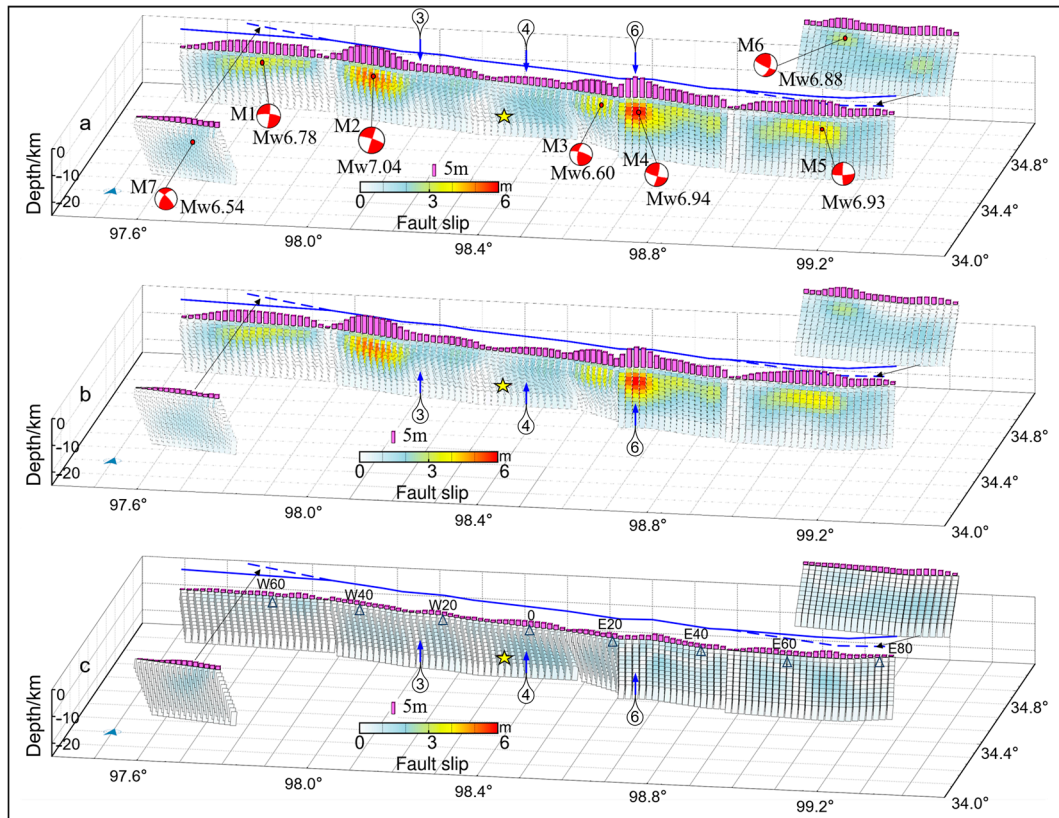


Figure 6. The preferred coseismic slip model of the 2021 Maduo earthquake. Coseismic slip distribution for the total (a), strike- (b), and dip-component (c) slip on the seismogenic fault. Pink bars indicate the maximum slip on the fault plane along the strike. The yellow star denotes the earthquake hypocenter. Red beach balls represent the focal mechanism solution of every asperity. Captions are as in Figure 3.

The coseismic slip model obtained from inversions of InSAR data (Figure 6) showed that the Maduo earthquake was dominated by a left-lateral strike-slip accompanied by a weak dip-slip component in local regions (Figures 6 and 7). The strike-slip and dip-slip components complemented each other in space. The strike-slip motion was significant and occurred at shallow depths, mostly above 10 km, with most of it reaching the surface (see Figures 6b and 7b). On the contrary, the dip-slip component was generally very small and mostly concentrated at depths of below 8 km, especially near fault stepovers or triple junctions (see Figures 6c and 7c). It may arise from a slip promoted by the interaction of faults or their growing junction at depth. Assuming a shear modulus of 30 GPa, the total seismic moment was 1.6×10^{20} N·m, equivalent to a magnitude of Mw 7.35. The seismic moments released by each asperity are listed in Table 2. Most of the seismic moment was released in the upper crust, from the surface to a depth of 10 km (Figure 7d). Overall, with the epicenter as the reference, a slip to the west was primarily distributed at shallower depths than to the east, while a slip on the subsidiary faults was deeper than on the main fault.

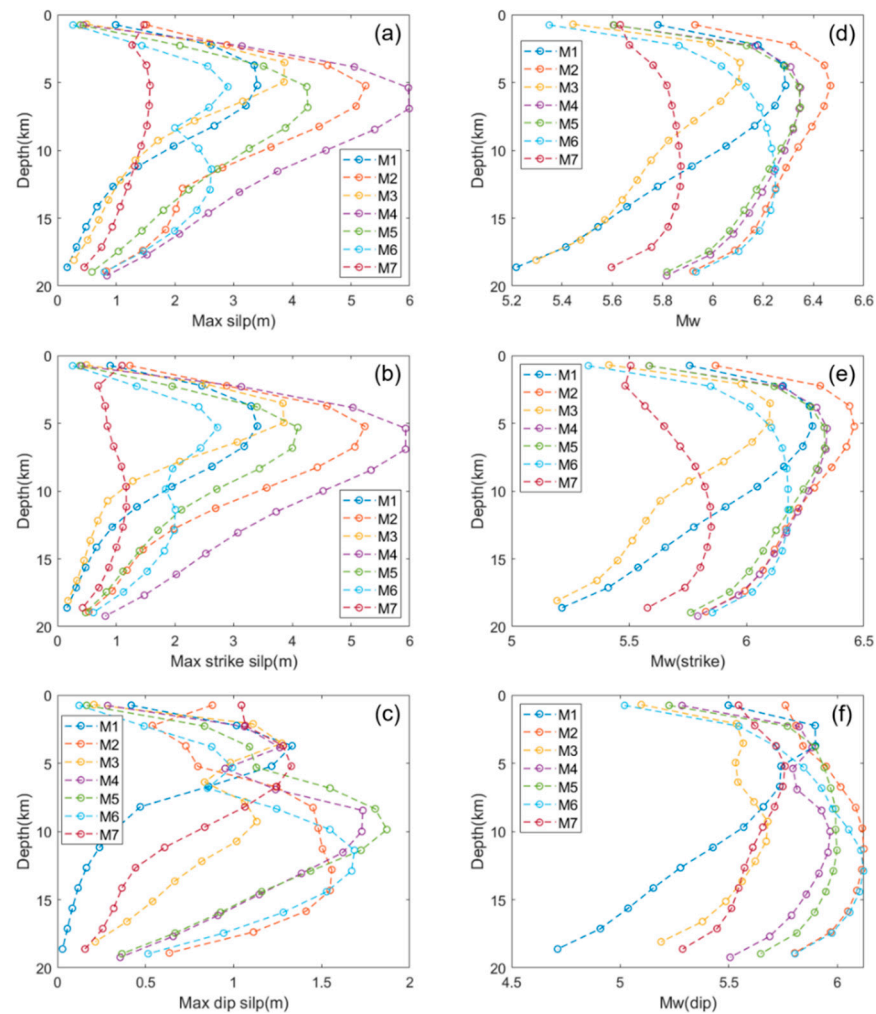


Figure 7. Distribution of released seismic moment and slip with depth. Distribution of the total (a), strike- (b), and dip-direction (c) slip-along depth for every asperity. Distribution of the total (d), strike- (e), and dip-direction (f) released seismic moment along depth for every asperity.

The coseismic slip on the fault plane was mainly distributed across seven asperities separated by four obvious slip gaps, five of which (M1–M5) were located on the main fault, while two (M6 and M7) were on branch faults (see Figure 5). The largest slip was ~6.0 m at a depth of 6–7 km, ~27 km east of the epicenter (M4; Table 2). This asperity was between the locations of the peak slip reported by [9,23]. The second largest peak had a slip of 5.3 m at a depth of ~5 km, ~35 km west of the epicenter (M2; Table 2), near the western fault branching (Figure 6c). Slips on the main fault with depth presented a pattern of unimodal distribution from the surface downward ~20 km (see Figure 7a). All peak slips in each asperity were concentrated at a depth of 5–6 km. The slip width increased gradually from west to east (Table 2). Slip distribution on the two rupture-end branches differed noticeably from that on the main fault. It exhibited a bimodal pattern, with two local peak slips at the shallow and deep locations, respectively. For instance, the primary and secondary peaks on M6 were 2.9 m at a depth of 5.3 km and 2.6 m at a depth of 12 km, respectively. In contrast, the maximum and secondary slips on M7 were equivalent in magnitude and occurred at a depth of ~5.2 km and the surface, respectively (Figure 6a). Specifically, the slip-on M7 did not appear to reach the surface.

4. Discussion

4.1. Deformation Patterns of Fault Steppers

The intricate geometric nature of the seismogenic fault was clearly demonstrated through detailed mapping of the surface rupture zone associated with the 2021 Maduo earthquake [5,6,46] (see Figure 2). Our UAV-based mapping of the surface rupture zones indicated that three EW-trending releasing stepovers, parallel to the contemporary maximum shear strain direction [10,47], were ruptured co-seismically (see Figure 8). Locally, the minimum amplitude of NS-direction optical and SAR displacement fields at EW-trending releasing stepovers indicated a reduction of effective normal stress while ruptures propagated through them, which facilitated rupture propagation [48].

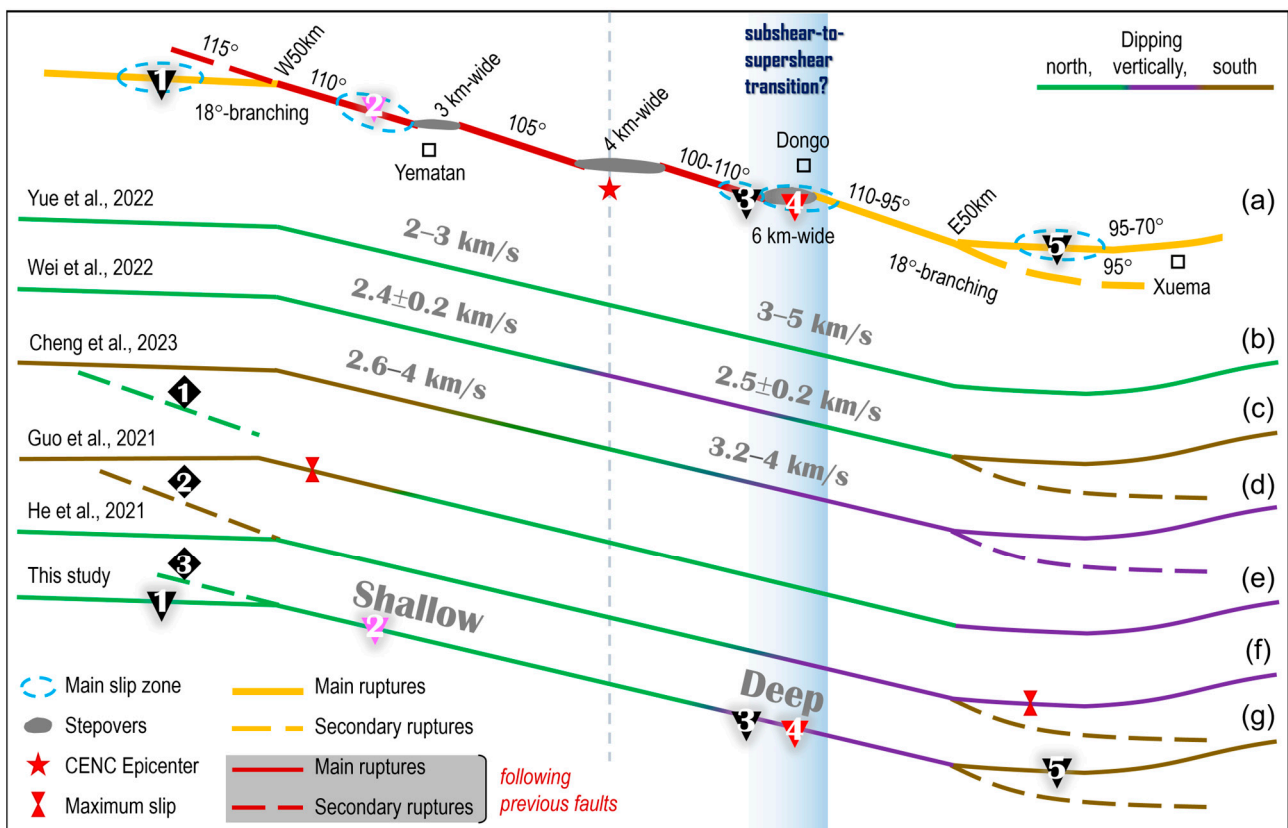


Figure 8. Simplified surface rupture zone (a) and seismogenic fault models used in the coseismic slip distribution inversion (b–g) of the 2021 Maduo earthquake [9,10,12,17,18]. The numbers show the rupture speeds of the western and eastern sections of the epicenter, respectively. The caption is as for Figure 2.

The stepover located 20–30 km east of the epicenter, the widest of the three, deserves a closer look. Previous studies have suggested that stepovers wider than 5 km tend to stop rupture propagation [49–51]. However, connecting structures within the stepover could increase the likelihood of a rupture jumping through [52,53]. Within this N90°E-trending stepover, two parallel surface rupture strands were observed, each with a narrow zone of less than 100 m width, 1 km apart, and a local peak surface offset of 2.5 m. These intermediate structures within the stepover (Figure 3e) may play a crucial role in facilitating a rupture breaching through this 6 km-wide stepover, supporting the findings of numerical models [48]. In a relatively immature structure, interactions between discontinuous and lateral faults may facilitate fault nucleation and growth, leading to fault linkage and coalescence [54].

4.2. Rupture Branching at the Western End

Our optical and SAR deformation fields showed a clear branching near the eastern end of the rupture. This eastern branching may be associated with the triggering a slip of a SE-trending secondary fault, which has been confirmed by aftershock seismicity [14] and field investigations [55], surface rupture zone mapping [6], and geodetic and seismogenic inversion results [9,18]. Less is known about the branching at the western end, where a subtle lineation striking N115°E appeared northwest of the main rupture, as shown in Figure 3g,h. The deformation discontinuity followed a preexisting fault east of the Eling Lake (Pink diamond 3 in Figure 2), as indicated on the geologic map [4], which received little attention in previous studies [17,18]. Models with a coseismic slip on the western fault branch improved the fit to the observed deformation field to some extent (refer to Table S2 and Figure S5 in the Supporting Information). Taking this side branch as the receiver fault in Coulomb stress calculation, a slip on the main fault as the driving source resulted in a small increase in the Coulomb failure stress on the receiver fault (Text S1 and Figure S4 in Supporting Information) [18], suggesting the potential for an additional increment of positive stress from the main shock static stress change [56].

Coseismic reactivation of the western branch is supported by geological investigations. During field reconnaissance on 5 June 2021 [4], we discovered distributed extensional fractures in loose sandy alluvium shortly after the earthquake. The cracks had a stable orientation of an EW trend in an en echelon arrangement, suggesting that these fractures arose from tectonic activity on the preexisting N115°E-trending fault rather than from collapses or strong ground shaking [4] (see Figure 2). No clear indicators show visible surface displacement across the cracks; however, it is not uncommon for secondary faults to reactivate with a nominal slip during the earthquake. For example, Xu et al. utilized full-resolution phase gradient maps to uncover minor deformations that are challenging to detect using the InSAR phase [28]. They interpreted these deformations as triggering slips on previously unidentified faults near the 2019 Ridgecrest earthquake sequence ruptures [57,58]. Similar off-fault diffused deformation characteristics were also observed during the 1992 Mw7.3 Landers earthquake [59], the 1999 Mw 7.1 Hector Mine earthquake [60], the 2020 Mw 6.5 Monte Cristo Range earthquake [61], the 2020 Mw 6.8 Elazığ earthquake [62], and others. These characteristics are consistently associated with the activation of faults near the causative fault or reactivation of pre-existing weakness zones [63–65].

The 2021 Maduo earthquake has been added to the global list of earthquakes with a ruptured bifurcation near the terminal of the causative fault [9,66,67]. Theoretical and numerical modeling results have shown that prestress conditions, rupture speed, and bifurcation angle impact the evolution of a fault bifurcation and lead to different bifurcation patterns [68–72], such as unilateral or bilateral bifurcation and static or dynamic stress triggering (Table 3). For example, during the 1992 Mw7.3 Landers earthquake, two secondary faults intersected the northern and southern ends of the main fault and were statically triggered simultaneously [59]. The 1999 Mw7.1 Hector Mine earthquake, on the other hand, was considered to have dynamically triggered two secondary ruptures on the northern and southern ends of the main fault. Coseismic fault branching in cross-section is also commonly observed on non-planar oblique and dip-slip faults and is found to play an important role in slip partitioning of the fault system [73–75]. However, the triggering mechanism of the western and eastern bifurcations remains unclear. Currently, the static-dynamic dual triggering model in nature is rarely reported. More work is needed to better understand the dynamic process of tail bifurcations of the 2021 Maduo earthquake.

Table 3. Published historic earthquakes with tail-end bifurcation.

Event	Bifurcation	N/E End	S/W End	Reference
1999 Mw7.1 Hector Mine earthquake	Unilateral	NE, uncertain		[76]
2002 Mw7.9 Denali earthquake	Unilateral		SW, uncertain	[77]
2003 Mw6.8 Zemmouri earthquake	Unilateral		SW, uncertain	[78]
2008 Mw7.9 Wenchuan earthquake	Unilateral		SW, static	[79]
2010 Mw 6.9 Yushu earthquake	Unilateral		W, uncertain	[14]
2015 M7.2 Sarez earthquake	Unilateral	E, dynamic		[37]
2016 M7.2 Kumamoto earthquake	Unilateral		SW, static	[80]
2016 Mw7.9 Kaikoura earthquake	Unilateral		SW, dynamic	[81]
2021 Ms7.4 Maduo earthquake	Unilateral	E, dynamic		[14]
2021 Ms7.4 Maduo earthquake	Unilateral		W, static	[17]
1992 Mw7.3 Landers earthquake	Bilateral	N, static	S, static	[59]
1999 M7.1 Hector Mine earthquake	Bilateral	N, dynamic	S, dynamic	[82]
2019 Ridgecrest earthquake sequence (Mw7.1 event)	Bilateral	NW, static	SE, static	[83]
2021 Ms7.4 Maduo earthquake	Bilateral	E	W	[18], This study

4.3. Sensitivity of Rupture Behaviors to Fault Heterogeneity

Our geodetic coseismic slip distribution exhibits an obvious asymmetry in slip depth and stress drop, which is the east-west contrast of the bilateral rupture, with the epicenter as the point of reference. The slip to the west mainly concentrated at shallower depths, with a smaller stress drop than that to the east (see Figure 9). The fault's dip angle steepened gradually towards the east, which was consistent with the relocated aftershock distribution [14]. Furthermore, this variation in slip depth along the fault was associated with the rupture velocity, as estimated from seismic waveforms [10]. Specifically, the rupture speed towards the west was slower than towards the east [9,10,12]. Interestingly, this spatial difference on both sides of the epicenter was also reflected by changes in the geometric and structural properties of the fault. Surface ruptures on the western side, beyond the EW-trending stepovers, aligned with a series of N110°-striking, stress-unfavorable, and older inherited faults. On the eastern side, beyond the surface ruptures of the initial 10 km section that overlap with one geologically mapped reverse fault, they followed with the structurally less mature but more optimally oriented faults of an N093°-striking, relative to the regional stress field [47]. A similar pattern was also observed for coseismic slip at more deep depths. Only the peak slip of the asperity M2 was located on the N110°-striking and older inherited fault, while all peak slips (i.e., main stress drop) of other asperities (M1, M3–M5) were released on the N093°-striking and optimally oriented faults. This observation supports the conclusion that the alignment of a fault with the stress field can have a more significant impact on rupture dynamics than other factors, such as fault structural simplicity, maturity, and strength [47].

The asymmetry of earthquake slips and rupture speeds strongly couples with along-strike changes in the geometric and structural properties of the fault, including dip direction and angle, degrees of geologic inheritance, and fault development to the east and west of the epicenter, which highlights the sensitivity of rupture behaviors to fault heterogeneity. Prior studies show that the largest slips and higher rupture speeds are most likely to occur on the most mature half of the ruptured fault section [84,85]. Although immature parts of a fault associated with high fault strength likely act as mechanical barriers to earthquake slip [86], there are exceptions. The 2020 Mw 6.8 Elazığ earthquake ruptured the Pürtürge segment of the East Anatolian fault, which has low-to-moderate structural maturity [62]. The largest slip occurred at a bend of about 10° and experienced the largest initial stress

(and consequently the largest stress drop) of 40 MPa, with very few aftershocks when the rupture approached this strong asperity at a locally supershear speed of ~ 4 km/s [87]. Similarly, the highest slip of the Maduo earthquake was released at the widest stepover with the largest stress drop of 42 MPa (Figure 9). The aftershock gap occurred east of this stepover [14] and was linked to the higher rupture speed (even reaching supershear velocity locally) [10–12]. Dynamic rupture models in heterogeneous media show that locally stronger fault sections, rather than slowing ruptures, drive them forward at velocities exceeding the shear wave speed [88]. As noted by Oglesby et al. [53], the connecting intermediate structures significantly enhance the ability of an earthquake rupture to propagate across the widest stepover, resulting in a larger event and potentially facilitating the subshear-to-supershear transition [89–91]. Although our results do not directly confirm the occurrence of the subshear-to-supershear transition at the widest stepover [12], which is favorably oriented in the background stress field, this possibility is still supported.

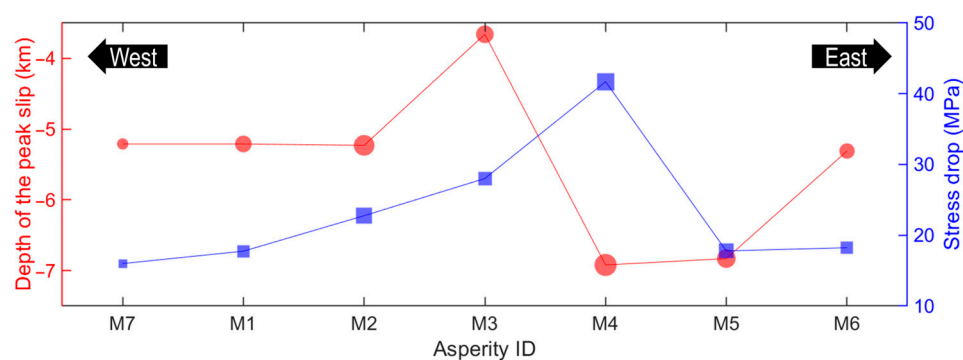


Figure 9. Stress drop and depth of the peak slip of every asperity for the optimal slip distribution model. The symbol size indicates the peak slip of every asperity.

5. Conclusions

In this study, we utilized SAR and optical displacement fields, along with on-fault surface rupture zone data, to precisely determine the geometric parameters of the fault associated with the 2021 Maduo earthquake. An adaptive quadtree downsampling method was employed to enhance the quality of the dataset utilized in the coseismic slip inversion. The optimized 3D slip model with varying strikes and dips revealed five main asperities. Most of the slip was concentrated primarily above 10 km, and no slip extended to depths greater than 20 km. The largest slip of ~ 6 m, with a depth of ~ 6.9 km, occurred near the widest stepover east of the epicenter, which was also located in the transition zone from sub-shear to super-shear rupture. Both optical and SAR displacement fields consistently indicated the evidence of local minimization of effective normal stress on releasing stepovers, which facilitated rupture through them. Connecting intermediate structures play a role in maintaining the propagation of ruptures through wide stepovers when they align with the optimal stress orientation and may even facilitate the transition from subshear to supershear. Our optical displacement fields, phase gradient fields, and geological investigations provide further evidence of coseismic reactivation of a branched fault at the western end. Furthermore, we found that there was a significant asymmetry in slip depth, stress drop, and rupture velocity to the east and west of the epicenter, which was coupled with variations in the geometric and structural characteristics of fault segments along the strike. Our findings highlight the impact of small-scale details of fault geometry on rupture behaviors.

Supplementary Materials: The following supporting information can be downloaded at <https://www.mdpi.com/article/10.3390/rs16040713/s1>, [18,23,92–97].

Author Contributions: Conceptualization, X.L., Z.J. and J.L.-Z.; Funding acquisition, X.L. and J.L.-Z.; Methodology, X.L., D.D., X.M. and Y.H.; Validation, Q.R. and J.L.; Writing—original draft, X.L. and

D.D.; Writing—review & editing, X.L., Z.J. and J.L.-Z. All authors have read and agreed to the published version of the manuscript.

Funding: This work was supported by Science for Earthquake Resilience, China Earthquake Administration (XH22003C), the Open Funding of National Field Scientific Observation and Research Station of Geophysics, Lhasa (NORSLS22-01), the Open Funding of National Field Scientific Observation and Research Station of Gravity and Earth tides, Wuhan (WHYWZ202201), the Basic Scientific Funding of Institute of Seismology, China Earthquake Administration (IS202226325), and the National Key Research and Development Program of China (2021YFC3000605).

Institutional Review Board Statement: Not applicable.

Informed Consent Statement: Not applicable.

Data Availability Statement: All Sentinel-1/2 data were downloaded from the European Space Agency (ESA) (<https://earthexplorer.usgs.gov/>, accessed on 17 October 2021). Atmospheric corrected data were downloaded from the Generic Atmospheric Correction Online Service for InSAR. The moment tensor solutions of the 2021 Maduo earthquake and the historical earthquakes on the Bayan-Har Block come from the Global Centroid Moment Tensor project (Global CMT; <http://www.globalcmt.org>, accessed on 21 June 2021) and the China Earthquake Data Center (CEDC, <http://data.earthquake.cn/index.html>, accessed on 21 June 2021).

Acknowledgments: Our thanks go to Tao Xia, Xin Li, Wenjun Kang, Aixia Dou, Rongjiang Wang, Xiaohua Xu, and Pengfei Yu for their help and discussions. Most figures were made using the public domain Generic Mapping Tools (Wessel and Smith, 1998).

Conflicts of Interest: The authors declare no conflicts of interest.

References

- Zhao, D.; Qu, C.; Chen, H.; Shan, X.; Song, X.; Gong, W. Tectonic and Geometric Control on Fault Kinematics of the 2021 Mw7.3 Maduo (China) Earthquake Inferred from Interseismic, Coseismic, and Postseismic InSAR Observations. *Geophys. Res. Lett.* **2021**, *48*, e2021GL095417. [CrossRef]
- Zhu, Y.; Diao, F.; Fu, Y.; Liu, C.; Xiong, X. Slip rate of the seismogenic fault of the 2021 Maduo earthquake in western China inferred from GPS observations. *Sci. China Earth Sci.* **2021**, *64*, 1363–1370. (In Chinese) [CrossRef]
- Pan, J.; Li, H.; Chevalier, M.-L.; Tapponnier, P.; Bai, M.; Li, C.; Liu, F.; Liu, D.; Wu, K.; Wang, P.; et al. Co-seismic rupture of the 2021, M7.4 Maduo earthquake (northern Tibet): Short-cutting of the Kunlun fault big bend. *Earth Planet. Sci. Lett.* **2022**, *594*, 117703. [CrossRef]
- Liu, X.; Xia, T.; Liu, Z.J.; Yao, W.; Xu, J.; Deng, D.; Han, L.; Jia, Z.; Shao, Y.; Wang, Y.; et al. Distributed Characteristics of the Surface Deformations Associated with the 2021 Mw7.4 Madoi Earthquake, Qinghai, China. *Seismol. Geol.* **2022**, *44*, 461–483. [CrossRef]
- Yuan, Z.; Li, T.; Su, P.; Sun, H.; Ha, G.; Guo, P.; Chen, G.; Thompson Jobe, J. Large Surface-Rupture Gaps and Low Surface Fault Slip of the 2021 Mw7.4 Maduo Earthquake along a Low-Activity Strike-Slip Fault, Tibetan Plateau. *Geophys. Res. Lett.* **2022**, *49*, e2021GL096874. [CrossRef]
- Liu-Zeng, J.; Yao, W.; Liu, X.; Shao, Y.; Wang, W.; Han, L.; Wang, Y.; Zeng, X.; Li, J.; Wang, Z.; et al. High-resolution structure-from-motion models covering 160 km-long surface ruptures of the 2021 MW 7.4 Madoi earthquake in northern Qinghai-Tibetan Plateau. *Earthq. Res. Adv.* **2022**, *2*, 100140. [CrossRef]
- Donald, L.W.; Coppersmith, K.J. New empirical relationships among magnitude, rupture length, rupture width, rupture area, and surface displacement. *Bull. Seismol. Soc. Am.* **1994**, *84*, 974–1002.
- Tapponnier, P.; Xu, Z.; Roger, F.; Meyer, B.; Arnaud, N.; Wittlinger, G.; Yang, J. Oblique stepwise rise and growth of the Tibet plateau. *Science* **2001**, *294*, 1671–1677. [CrossRef]
- Wei, S.; Zeng, H.; Shi, Q.; Liu, J.; Luo, H.; Hu, W.; Li, Y.; Wang, W.; Ma, Z.; Liu-Zeng, J.; et al. Simultaneous Rupture Propagation Through Fault Bifurcation of the 2021 Mw7.4 Maduo Earthquake. *Geophys. Res. Lett.* **2022**, *49*, e2022GL100283. [CrossRef]
- Yue, H.; Shen, Z.-K.; Zhao, Z.; Wang, T.; Cao, B.; Li, Z.; Bao, X.; Zhao, L.; Song, X.; Ge, Z.; et al. Rupture process of the 2021 M7.4 Maduo earthquake and implication for deformation mode of the Songpan-Ganzi terrane in Tibetan Plateau. *Proc. Natl. Acad. Sci. USA* **2022**, *119*, e2116445119. [CrossRef]
- Zhang, X.; Feng, W.; Du, H.; Samsonov, S.; Yi, L. Supershear Rupture during the 2021 MW 7.4 Maduo, China, Earthquake. *Geophys. Res. Lett.* **2022**, *49*, e2022GL097984. [CrossRef]
- Cheng, C.; Wang, D.; Yao, Q.; Fang, L.; Xu, S.; Huang, Z.; Liu, T.; Wang, Z.; Huang, X. The 2021 Mw 7.3 Madoi, China Earthquake: Transient Supershear Ruptures on a Presumed Immature Strike-Slip Fault. *J. Geophys. Res. Solid Earth* **2023**, *128*, e2022JB024641. [CrossRef]

13. Chen, K.; Avouac, J.-P.; Geng, J.; Liang, C.; Zhang, Z.; Li, Z.; Zhang, S. The 2021 Mw 7.4 Madoi Earthquake: An Archetype Bilateral Slip-Pulse Rupture Arrested at a Splay Fault. *Geophys. Res. Lett.* **2022**, *49*, e2021GL095243. [[CrossRef](#)]
14. Wang, W.; Fang, L.; Wu, J.; Tu, H.; Chen, L.; Lai, G.; Zhang, L. Aftershock sequence relocation of the 2021 MS7.4 Maduo Earthquake, Qinghai, China. *Sci. China Earth Sci.* **2021**, *51*, 1193–1202. [[CrossRef](#)]
15. Li, C.; Li, T.; Hollingsworth, J.; Zhang, Y.; Qian, L.; Shan, X. Strain Threshold for the Formation of Coseismic Surface Rupture. *Geophys. Res. Lett.* **2023**, *50*, e2023GL103666. [[CrossRef](#)]
16. He, K.; Wen, Y.; Xu, C.; Zhao, Y. Fault Geometry and Slip Distribution of the 2021 Mw 7.4 Maduo, China, Earthquake Inferred from InSAR Measurements and Relocated Aftershocks. *Seismol. Res. Lett.* **2021**, *93*, 8–20. [[CrossRef](#)]
17. Guo, R.; Yang, H.; Li, Y.; Zheng, Y.; Zhang, L. Complex Slip Distribution of the 2021 Mw 7.4 Maduo, China, Earthquake: An Event Occurring on the Slowly Slipping Fault. *Seismol. Res. Lett.* **2021**, *93*, 653–665. [[CrossRef](#)]
18. He, L.; Feng, G.; Wu, X.; Lu, H.; Xu, W.; Wang, Y.; Liu, J.; Hu, J.; Li, Z. Coseismic and Early Postseismic Slip Models of the 2021 Mw 7.4 Maduo Earthquake (Western China) Estimated by Space-Based Geodetic Data. *Geophys. Res. Lett.* **2021**, *48*, e2021GL095860. [[CrossRef](#)]
19. Li, Z.; Ding, K.; Zhang, P.; Wen, Y.; Zhao, L.; Chen, J. Coseismic Deformation and Slip Distribution of 2021 Mw 7.4 Madoi Earthquake from GNSS Observation. *Geomat. Inf. Sci. Wuhan Univ.* **2021**, *46*, 1489. [[CrossRef](#)]
20. Jin, Z.; Fialko, Y. Coseismic and Early Postseismic Deformation Due to the 2021 M7.4 Maduo (China) Earthquake. *Geophys. Res. Lett.* **2021**, *48*, e2021GL095213. [[CrossRef](#)]
21. Xu, X.; Tong, X.; Sandwell, D.T.; Milliner, C.W.D.; Dolan, J.F.; Hollingsworth, J.; Leprince, S.; Ayoub, F. Refining the shallow slip deficit. *Geophys. J. Int.* **2016**, *204*, 1843–1862. [[CrossRef](#)]
22. Milliner, C.W.D.; Sammis, C.; Allam, A.A.; Dolan, J.F.; Hollingsworth, J.; Leprince, S.; Ayoub, F. Resolving Fine-Scale Heterogeneity of Co-seismic Slip and the Relation to Fault Structure. *Sci. Rep.* **2016**, *6*, 27201. [[CrossRef](#)] [[PubMed](#)]
23. Xiong, W.; Chen, W.; Wang, D.; Wen, Y.; Nie, Z.; Liu, G.; Dijin, W.; Yu, P.; Qiao, X.; Zhao, B. Coseismic slip and early afterslip of the 2021 Mw 7.4 Maduo, China earthquake constrained by GPS and InSAR data. *Tectonophysics* **2022**, *840*, 229558. [[CrossRef](#)]
24. Guo, H.; Lay, T.; Brodsky, E.E. Seismological Indicators of Geologically Inferred Fault Maturity. *J. Geophys. Res. Solid Earth* **2023**, *128*, e2023JB027096. [[CrossRef](#)]
25. Leprince, S.; Barbot, S.; Ayoub, F.; Avouac, J.P. Automatic and Precise Orthorectification, Coregistration, and Subpixel Correlation of Satellite Images, Application to Ground Deformation Measurements. *IEEE Trans. Geosci. Remote Sens.* **2007**, *45*, 1529–1558. [[CrossRef](#)]
26. Huang, Y.; Liu, X.; Mo, X.; Deng, D.; Ruan, Q.; Liu, J.; Jia, Z. Coseismic Deformation Extration Method and Geodynamic Significances of Displacement Gradients Based on Optical Imagery. *J. Geod. Geodyn.* **2023**, *in press*.
27. Sandwell, D.T.; Price, E.J. Phase gradient approach to stacking interferograms. *J. Geophys. Res. Solid Earth* **1998**, *103*, 30183–30204. [[CrossRef](#)]
28. Xu, X.; Sandwell, D.; Smith-Konter, B. Coseismic Displacements and Surface Fractures from Sentinel-1 InSAR: 2019 Ridgecrest Earthquakes. *Seismol. Res. Lett.* **2020**, *91*, 1979–1985. [[CrossRef](#)]
29. Sandwell, D.; Mellors, R.; Tong, X.; Wei, M.; Wessel, P. Open radar interferometry software for mapping surface Deformation. *Eos Trans. Am. Geophys. Union* **2011**, *92*, 234. [[CrossRef](#)]
30. Yu, C.; Li, Z.; Penna, N.T. Interferometric synthetic aperture radar atmospheric correction using a GPS-based iterative tropospheric decomposition model. *Remote Sens. Environ.* **2017**, *204*, 109–121. [[CrossRef](#)]
31. Yu, C.; Li, Z.; Penna, N.T.; Crippa, P. Generic Atmospheric Correction Model for Interferometric Synthetic Aperture Radar Observations. *J. Geophys. Res. Solid Earth* **2018**, *123*, 9202–9222. [[CrossRef](#)]
32. Hanssen, R.F. *Radar Interferometry Data Interpretation and Error Analysis*; Springer: Berlin/Heidelberg, Germany, 2001.
33. Zhu, J.; Li, Z.; Hu, J. Research Progress and Methods of InSAR for Deformation Monitoring. *Acta Geod. Cartogr. Sin.* **2017**, *46*, 1717.
34. He, P.; Wen, Y.; Xu, C.; Chen, Y. High-quality three-dimensional displacement fields from new-generation SAR imagery: Application to the 2017 Ezgeleh, Iran, earthquake. *J. Geod.* **2019**, *93*, 573–591. [[CrossRef](#)]
35. Fialko, Y.; Simons, M.; Agnew, D. The complete (3-D) surface displacement field in the epicentral area of the 1999 MW7.1 Hector Mine Earthquake, California, from space geodetic observations. *Geophys. Res. Lett.* **2001**, *28*, 3063–3066. [[CrossRef](#)]
36. Mo, X.; Jia, Z.; Deng, D.; Huang, Y.; Liu, J.; Ruan, q.; Liu, X. An Adaptive Quadtree Downsampling Method based on Deformation Gradient and Coherence for InSAR Data. *Earthq. Res. China* **2023**. *in review*.
37. Jin, Z. Lithospheric deformation due to the 2015 M7.2 Sarez (Pamir) earthquake constrained by 5 years of space geodetic observations. *J. Geophys. Res. Solid Earth* **2022**, *127*, e2021JB022461. [[CrossRef](#)]
38. Milliner, C.; Donnellan, A.; Aati, S.; Avouac, J.-P.; Zinke, R.; Dolan, J.F.; Wang, K.; Bürgmann, R. Bookshelf Kinematics and the Effect of Dilatation on Fault Zone Inelastic Deformation: Examples from Optical Image Correlation Measurements of the 2019 Ridgecrest Earthquake Sequence. *J. Geophys. Res. Solid Earth* **2021**, *126*, e2020JB020551. [[CrossRef](#)]
39. Choi, E.; Seeber, L.; Steckler, M.S.; Buck, R. One-sided transform basins and “inverted curtains”: Implications for releasing bends along strike-slip faults. *Tectonics* **2011**, *30*, TC6006. [[CrossRef](#)]
40. Lozos, J.C.; Oglesby, D.D.; Brune, J.N.; Olsen, K.B. Rupture Propagation and Ground Motion of Strike-Slip Steppers with Intermediate Fault Segments. *Bull. Seismol. Soc. Am.* **2015**, *105*, 387–399. [[CrossRef](#)]

41. Jin, Z.; Fialko, Y.; Yang, H.; Li, Y. Transient Deformation Excited by the 2021 M7.4 Maduo (China) Earthquake: Evidence of a Deep Shear Zone. *J. Geophys. Res. Solid Earth* **2023**, *128*, e2023JB026643. [[CrossRef](#)]
42. Wang, R.; Schurr, B.; Milkereit, C.; Shao, Z.; Jin, M. An improved automatic scheme for empirical baseline correction of digital strong-motion records. *Bull. Seismol. Soc. Am.* **2011**, *101*, 2029–2044. [[CrossRef](#)]
43. Jia, S.; Guo, W.; Mooney, W.D.; Wang, F.; Liu, Z. Crustal structure of the middle segment of the Qilian fold belt and the coupling mechanism of its associated basin and range system. *Tectonophysics* **2019**, *770*, 128154. [[CrossRef](#)]
44. Kaneko, Y.; Hamling, I.J.; Van Dissen, R.J.; Motagh, M.; Samsonov, S.V. InSAR imaging of displacement on flexural-slip faults triggered by the 2013 Mw 6.6 Lake Grassmere earthquake, central New Zealand. *Geophys. Res. Lett.* **2015**, *42*, 781–788. [[CrossRef](#)]
45. USGS. *Earthquake Catalog Released by U. S. Geological Survey*; Earthquake Science Center: New York, NY, USA, 2021.
46. Pan, J.; Bai, M.; Li, C.; Liu, F.; Li, H.; Liu, D.; Marie-Luce, C.; Wu, K.; Wang, P.; Lu, H.; et al. Coseismic surface rupture and seismogenic structure of the 2021-05-22 Maduo(Qinghai)Ms7.4 earthquake. *Acta Geol. Sin.* **2021**, *95*, 1655–1670. (In Chinese) [[CrossRef](#)]
47. Liu-Zeng, J.; Liu, Z.; Liu, X.; Milliner, C.; Avouac, J.-P.; Padilla, A.R.; Xu, S.; Yao, W.; Klinger, Y.; Han, L.; et al. Fault orientation trumps fault maturity in controlling coseismic rupture characteristics of the 2021 Maduo earthquake. *AGU Adv.* **2023**. *in review*.
48. Lozos, J.C.; Oglesby, D.D.; Brune, J.N.; Olsen, K.B. Small intermediate fault segments can either aid or hinder rupture propagation at stepovers. *Geophys. Res. Lett.* **2012**, *39*, L18305. [[CrossRef](#)]
49. King, G.; Klinger, Y.; Bowman, D.; Tapponnier, P. Slip-partitioned surface breaks for the M w 7.8 2001 Kokoxili earthquake, China. *Bull. Seismol. Soc. Am.* **2005**, *95*, 731–738. [[CrossRef](#)]
50. Klinger, Y. Relation between continental strike-slip earthquake segmentation and thickness of the crust. *J. Geophys. Res. Solid Earth* **2010**, *115*, B07306. [[CrossRef](#)]
51. Wesnousky, S.G. Predicting the endpoints of earthquake ruptures. *Nature* **2006**, *444*, 358–360. [[CrossRef](#)]
52. Liu-Zeng, J.; Sun, J.; Wang, P.; Hudnut, K.W.; Ji, C.; Zhang, Z.; Xu, Q.; Wen, L. Surface ruptures on the transverse Xiaoyudong fault: A significant segment boundary breached during the 2008 Wenchuan earthquake, China. *Tectonophysics* **2012**, *580*, 218–241. [[CrossRef](#)]
53. Oglesby, D.D. The Dynamics of Strike-Slip Step-Overs with Linking Dip-Slip Faults. *Bull. Seismol. Soc. Am.* **2005**, *95*, 1604–1622. [[CrossRef](#)]
54. Scholz, C.H. *The Mechanics of Earthquakes and Faulting*, 3rd ed.; Cambridge University Press: Cambridge, UK, 2019.
55. Yao, W.-Q.; Wang, Z.-J.; Liu-Zeng, J.; Liu, X.-L.; Han, L.-F.; Shao, Y.-X.; Wang, W.-X.; Xu, J.; Qin, K.-X.; Gao, Y.-P.; et al. Discussion on coseismic surface rupture length of the 2021 Mw 7.4 Maduo earthquake, Qinghai, China. *Seismol. Geol.* **2022**, *44*, 541–559.
56. Hardebeck, J.L. The impact of static stress change, dynamic stress change, and the background stress on aftershock focal mechanisms. *J. Geophys. Res. Solid Earth* **2014**, *119*, 8239–8266. [[CrossRef](#)]
57. Ponti, D.J.; Blair, J.L.; Rosa, C.M.; Thomas, K.; Pickering, A.J.; Akciz, S.; Angster, S.; Avouac, J.-P.; Bachhuber, J.; Bacon, S.; et al. Documentation of Surface Fault Rupture and Ground-Deformation Features Produced by the 4 and 5 July 2019 Mw 6.4 and Mw 7.1 Ridgecrest Earthquake Sequence. *Seismol. Res. Lett.* **2020**, *91*, 2942–2959. [[CrossRef](#)]
58. Thompson Jobe, J.A.; Philibosian, B.; Chupik, C.; Dawson, T.; Bennett, S.E.K.; Gold, R.; DuRoss, C.; Ladinsky, T.; Kendrick, K.; Haddon, E.; et al. Evidence of Previous Faulting along the 2019 Ridgecrest, California, Earthquake Ruptures. *Bull. Seismol. Soc. Am.* **2020**, *110*, 1427–1456. [[CrossRef](#)]
59. Fialko, Y. Probing the mechanical properties of seismically active crust with space geodesy: Study of the coseismic deformation due to the 1992 Mw7.3 Landers (southern California) earthquake. *J. Geophys. Res. Solid Earth* **2004**, *109*, B03307. [[CrossRef](#)]
60. Sandwell, D.T.; Sichoix, L.; Agnew, D.; Bock, Y.; Minster, J.-B. Near real-time radar interferometry of the Mw 7.1 Hector Mine Earthquake. *Geophys. Res. Lett.* **2000**, *27*, 3101–3104. [[CrossRef](#)]
61. Koehler, R.D.; Dee, S.; Elliott, A.; Hatem, A.; Pickering, A.; Pierce, I.; Seitz, G. Field Response and Surface-Rupture Characteristics of the 2020 M 6.5 Monte Cristo Range Earthquake, Central Walker Lane, Nevada. *Seismol. Res. Lett.* **2021**, *92*, 823–839. [[CrossRef](#)]
62. Pousse-Beltran, L.; Nissen, E.; Bergman, E.A.; Cambaz, M.D.; Gaudreau, É.; Karasözen, E.; Tan, F. The 2020 Mw 6.8 Elazığ (Turkey) Earthquake Reveals Rupture Behavior of the East Anatolian Fault. *Geophys. Res. Lett.* **2020**, *47*, e2020GL088136. [[CrossRef](#)]
63. Petersen, M.D.; Dawson, T.E.; Chen, R.; Cao, T.; Wills, C.J.; Schwartz, D.P.; Frankel, A.D. Fault Displacement Hazard for Strike-Slip Faults. *Bull. Seismol. Soc. Am.* **2011**, *101*, 805–825. [[CrossRef](#)]
64. Livio, F.; Serva, L.; Gürpınar, A. Locating distributed faulting: Contributions from InSAR imaging to Probabilistic Fault Displacement Hazard Analysis (PFDHA). *Quat. Int.* **2017**, *451*, 223–233. [[CrossRef](#)]
65. Liu, J.; Sieh, K.; Hauksson, E. A structural interpretation of the aftershock “cloud” of the 1992 Mw 7.3 Landers earthquake. *Bull. Seismol. Soc. Am.* **2003**, *93*, 1333–1344. [[CrossRef](#)]
66. Sieh, K.; Jones, L.; Hauksson, E.; Hudnut, K.; Eberhart-Phillips, D.; Heaton, T.; Hough, S.; Hutton, K.; Kanamori, H.; Lilje, A.; et al. Near-field investigations of the landers earthquake sequence, April to July 1992. *Science* **1993**, *260*, 171–176. [[CrossRef](#)]
67. Baize, S.; Nurminen, F.; Sarmiento, A.; Dawson, T.; Takao, M.; Scotti, O.; Azuma, T.; Boncio, P.; Champenois, J.; Cinti, F.R.; et al. A Worldwide and Unified Database of Surface Ruptures (SURE) for Fault Displacement Hazard Analyses. *Seismol. Res. Lett.* **2019**, *91*, 499–520. [[CrossRef](#)]

68. Aochi, H.; Madariaga, R.; Fukuyama, E. Effect of normal stress during rupture propagation along nonplanar faults. *J. Geophys. Res. Solid Earth* **2002**, *107*, ESE 5-1–ESE 5-10. [[CrossRef](#)]
69. Duan, B.; Oglesby, D.D. Nonuniform prestress from prior earthquakes and the effect on dynamics of branched fault systems. *J. Geophys. Res.* **2007**, *112*, B05308. [[CrossRef](#)]
70. Kame, N.; Rice, J.R.; Dmowska, R. Effects of prestress state and rupture velocity on dynamic fault branching. *J. Geophys. Res. Solid Earth* **2003**, *108*, B52265. [[CrossRef](#)]
71. Poliakov, A.N.B.; Dmowska, R.; Rice, J.R. Dynamic shear rupture interactions with fault bends and off-axis secondary faulting. *J. Geophys. Res. Solid Earth* **2002**, *107*, ESE 6-1–ESE 6-18. [[CrossRef](#)]
72. Douilly, R.; Oglesby, D.D.; Cooke, M.L.; Hatch, J.L. Dynamic models of earthquake rupture along branch faults of the eastern San Geronio Pass region in California using complex fault structure. *Geosphere* **2020**, *16*, 474–489. [[CrossRef](#)]
73. Liu-Zeng, J.; Zhang, Z.; Wen, L.; Tapponnier, P.; Sun, J.; Xing, X.; Hu, G.; Xu, Q.; Zeng, L.; Ding, L.; et al. Co-seismic ruptures of the 12 May 2008, Ms 8.0 Wenchuan earthquake, Sichuan: East–west crustal shortening on oblique, parallel thrusts along the eastern edge of Tibet. *Earth Planet. Sci. Lett.* **2009**, *286*, 355–370. [[CrossRef](#)]
74. Klinger, Y.; Xu, X.; Tapponnier, P.; Van der Woerd, J.; Lasserre, C.; King, G. High-Resolution Satellite Imagery Mapping of the Surface Rupture and Slip Distribution of the Mw ~7.8, 14 November 2001 Kokoxili Earthquake, Kunlun Fault, Northern Tibet, China. *Bull. Seismol. Soc. Am.* **2005**, *95*, 1970–1987. [[CrossRef](#)]
75. Park, J.-O.; Tsuru, T.; Kodaira, S.; Cummins, P.R.; Kaneda, Y. Splay Fault Branching along the Nankai Subduction Zone. *Science* **2002**, *297*, 1157–1160. [[CrossRef](#)] [[PubMed](#)]
76. Jonsson, S. Fault Slip Distribution of the 1999 Mw 7.1 Hector Mine, California, Earthquake, Estimated from Satellite Radar and GPS Measurements. *Bull. Seismol. Soc. Am.* **2002**, *92*, 1377–1389. [[CrossRef](#)]
77. Hreinsdóttir, S.; Freymueller, J.T.; Bürgmann, R.; Mitchell, J. Coseismic deformation of the 2002 Denali Fault earthquake: Insights from GPS measurements. *J. Geophys. Res. Solid Earth* **2006**, *111*, B03308. [[CrossRef](#)]
78. Ayadi, A.; Dorbath, C.; Ousadou, F.; Maouche, S.; Chikh, M.; Bounif, M.A.; Meghraoui, M. Zemmouri earthquake rupture zone (Mw 6.8, Algeria): Aftershocks sequence relocation and 3D velocity model. *J. Geophys. Res. Solid Earth* **2008**, *113*, B09301. [[CrossRef](#)]
79. Tang, R.; Zhu, S.; Gan, L. Dynamic Rupture Simulations of the 2008 7.9 Wenchuan Earthquake: Implication for Heterogeneous Initial Stress and Complex Multifault Geometry. *J. Geophys. Res. Solid Earth* **2021**, *126*, e2021JB022457. [[CrossRef](#)]
80. Hao, J.; Ji, C.; Yao, Z. Slip history of the 2016 Mw 7.0 Kumamoto earthquake: Intraplate rupture in complex tectonic environment. *Geophys. Res. Lett.* **2017**, *44*, 743–750. [[CrossRef](#)]
81. Ando, R.; Kaneko, Y. Dynamic Rupture Simulation Reproduces Spontaneous Multifault Rupture and Arrest during the 2016 Mw 7.9 Kaikoura Earthquake. *Geophys. Res. Lett.* **2018**, *45*, 12875–12883. [[CrossRef](#)]
82. Li, Y.-G.; Vidale, J.E.; Oglesby, D.D.; Day, S.M.; Cochran, E. Multiple-fault rupture of the M7.1 Hector Mine, California, earthquake from fault zone trapped waves. *J. Geophys. Res. Solid Earth* **2003**, *108*, B32165. [[CrossRef](#)]
83. Feng, W.; Samsonov, S.; Qiu, Q.; Wang, Y.; Zhang, P.; Li, T.; Zheng, W. Orthogonal Fault Rupture and Rapid Postseismic Deformation Following 2019 Ridgecrest, California, Earthquake Sequence Revealed from Geodetic Observations. *Geophys. Res. Lett.* **2020**, *47*, e2019GL086888. [[CrossRef](#)]
84. Perrin, C.; Manighetti, L.; Ampuero, J.-P.; Cappa, F.; Gaudemer, Y. Location of largest earthquake slip and fast rupture controlled by along-strike change in fault structural maturity due to fault growth. *J. Geophys. Res. Solid Earth* **2016**, *121*, 3666–3685. [[CrossRef](#)]
85. Socquet, A.; Hollingsworth, J.; Pathier, E.; Bouchon, M. Evidence of supershear during the 2018 magnitude 7.5 Palu earthquake from space geodesy. *Nat. Geosci.* **2019**, *12*, 192–199. [[CrossRef](#)]
86. Scholz, C.; Lawler, T. Slip tapers at the tips of faults and earthquake ruptures. *Geophys. Res. Lett.* **2004**, *31*, L21609. [[CrossRef](#)]
87. Gallovič, F.; Zahradník, J.; Plicka, V.; Sokos, E.; Evangelidis, C.; Fountoulakis, I.; Turhan, F. Complex rupture dynamics on an immature fault during the 2020 Mw 6.8 Elazığ earthquake, Turkey. *Commun. Earth Environ.* **2020**, *1*, 40. [[CrossRef](#)]
88. Dunham, E.M.; Favreau, P.; Carlson, J.M. A Supershear Transition Mechanism for Cracks. *Science* **2003**, *299*, 1557–1559. [[CrossRef](#)]
89. Bruhat, L.; Fang, Z.; Dunham, E.M. Rupture complexity and the supershear transition on rough faults. *J. Geophys. Res. Solid Earth* **2016**, *121*, 210–224. [[CrossRef](#)]
90. Hu, F.; Xu, J.; Zhang, Z.; Chen, X. Supershear transition mechanism induced by step over geometry. *J. Geophys. Res. Solid Earth* **2016**, *121*, 8738–8749. [[CrossRef](#)]
91. Ryan, K.J.; Oglesby, D.D. Dynamically modeling fault step overs using various friction laws. *J. Geophys. Res. Solid Earth* **2014**, *119*, 5814–5829. [[CrossRef](#)]
92. Parsons, T.; Stein, R.S.; Simpson, R.W.; Reasenber, P.A. Stress sensitivity of fault seismicity: A comparison between limited-offset oblique and major strike-slip faults. *J. Geophys. Res. Solid Earth* **1999**, *104*, 20183–20202. [[CrossRef](#)]
93. Xiong, X.; Shan, B.; Yong, Z.; Wang, R. Stress transfer and its implication for earthquake hazard on the Kunlun Fault, Tibet. *Tectonophysics* **2010**, *482*, 216–225. [[CrossRef](#)]
94. Yoshimitsu, O. Internal deformation due to shear and tensile faults in a half-space. *Bull. Seismol. Soc. Am.* **1992**, *82*, 1018–1040.
95. Wang, R.; Lorenzo-Martín, F.; Roth, F. PSGRN/PSCMP—A new code for calculating co- and post-seismic deformation, geoid and gravity changes based on the viscoelastic-gravitational dislocation theory. *Comput. Geosci.* **2006**, *32*, 527–541. [[CrossRef](#)]

-
96. Fang, J.; Ou, Q.; Wright, T.J.; Okuwaki, R.; Amey, R.M.J.; Craig, T.J.; Elliott, J.R.; Hooper, A.; Lazecký, M.; Maghsoudi, Y. Earthquake Cycle Deformation Associated with the 2021 MW 7.4 Madoo (Eastern Tibet) Earthquake: An Intraplank Rupture Event on a Slow-Slipping Fault from Sentinel-1 InSAR and Teleseismic Data. *J. Geophys. Res. Solid Earth* **2022**, *127*, e2022JB024268. [[CrossRef](#)]
 97. Zhao, L.; Xu, W.; Fang, N.; Liu, J.; Feng, G. Coseismic and early postseismic fault slip model and the seismogenic fault friction properties of the 2021 Qinghai Madoi Mw7.3 earthquake. *Chin. J. Geophys.* **2023**, *66*, 1086–1097. (In Chinese)

Disclaimer/Publisher’s Note: The statements, opinions and data contained in all publications are solely those of the individual author(s) and contributor(s) and not of MDPI and/or the editor(s). MDPI and/or the editor(s) disclaim responsibility for any injury to people or property resulting from any ideas, methods, instructions or products referred to in the content.